Materials Today Chemistry 32 (2023) 101641

Contents lists available at ScienceDirect

Materials Today Chemistry

journal homepage: www.journals.elsevier.com/materials-today-chemistry/

Efficient adsorption and photocatalytic degradation of organic contaminants using $TiO_2/(Bi_2O_3/Bi_2O_{2.33})$ nanotubes

R. Lu [a], S.-Z. Zhao [a], Y. Yang [a], Y. Wang [a], H.-L. Huang [a], Y.-D. Hu [b], R.D. Rodriguez [c], J.-J. Chen [a, *]

[a] *School of Materials and Energy, University of Electronic Science and Technology of China, Chengdu 610054, PR China*
[b] *School of Integrated Circuit Science and Engineering, University of Electronic Science and Technology of China, Chengdu 610054, PR China*
[c] *Tomsk Polytechnic University, 30 Lenin Ave, 634050, Tomsk, Russia*

ARTICLE INFO

Article history:
Received 4 February 2023
Received in revised form
16 June 2023
Accepted 26 June 2023
Available online xxx

Keywords:
Heterostructure
Photocatalysis degradation
Adsorption
Organic pollutant

ABSTRACT

TiO_2 nanotubes decorated with $Bi_2O_3/Bi_2O_{2.33}$ nanosheets were prepared through a facile avenue that combines sacrifice template and hydrothermal methods. The TiO_2 nanotube structure provided a large specific surface area, and the $TiO_2/(Bi_2O_3/Bi_2O_{2.33})$ heterojunction broadened the light absorption range by reducing the bandgap to 2.746 eV. The $TiO_2/(Bi_2O_3/Bi_2O_{2.33})$ heterostructure demonstrated high adsorption capability for methyl orange (100 mg/L) with a 70% adsorption rate after 60 min. The photocatalytic performance of the $TiO_2/(Bi_2O_3/Bi_2O_{2.33})$ heterostructure was evaluated through the degradation of rhodamine B (RhB) and tetracycline hydrochloride (TCH). The removal rates of RhB (10 mg/L) and high concentration TCH (50 mg/L) could reach 93% and 96% after 60 min and 120 min of light irradiation, respectively. Theoretical calculations showed that the $TiO_2/(Bi_2O_3/Bi_2O_{2.33})$ structure enhanced photogenerated charge separation, leading to improved degradation of organic pollutants. This study provides a facile way for designing and creating heterostructural nanotubes with enhanced performance for removing organic pollutants.

1. Introduction

After decades of rapid industrial development, the harmful organic contaminants in water are poisoning humans and the environment. Several methods, such as adsorption [1], photocatalytic degradation [2], electrocatalytic degradation [3], wet air oxidation [4], and so on, have been developed to remove pollutants. However, using single functional materials to remove contaminants often has the problem of low efficiency or secondary pollution (such as the adsorption method). Therefore, many efforts have been devoted to exploring multifunctional materials that integrate adsorption functions and photocatalytic degradation through structural design or component regulation [5].

As a multi-purpose semiconductor, titanium dioxide (TiO_2) has been demonstrated to be a promising candidate material for photocatalytic degradation of organic pollutants due to its chemical durability, environmental friendliness, and high photoactivity [6]. However, the high recombination rate of electron-hole pairs and low absorption of visible light severely impede the further development of TiO_2 in the field of photocatalysis [7]. To solve these problems, heterostructure is introduced. The internal electric field from heterostructure can help the rapid separation of electron-hole pairs, and the reduced bandgap caused by heterostructure enhances visible light absorption. In addition, morphological regulation can also have a positive impact on pollutant removal. Different TiO_2 nanostructures are made for better photocatalytic efficiency, such as nanoparticles [8], nanosheets [9], nanobelts [10] and nanotubes [11]. Among these nanomaterials, TiO_2 nanotubes should be given special attention because of their large specific surface area and high light absorption caused by multiple scattering events intrinsic to tubular structures.

Bismuth oxide (Bi_2O_3) possesses four different crystal forms—α, β, γ, and δ, and nonstoichiometric phases $Bi_2O_{0.75}$ and $Bi_2O_{2.33}$ [12]. Among them, $Bi_2O_{2.33}$ was demonstrated to have the adsorption capability for particular ions [13], and β-Bi_2O_3 exhibits a good response to visible light for photocatalysis with a bandgap of 2.3 eV. Furthermore, the TiO_2 and Bi_2O_3 heterostructures could help accelerate the separation of photo-generated carriers, enhancing

---

[*] Corresponding author.
E-mail address: jinjuchen@uestc.edu.cn (J.-J. Chen).

https://doi.org/10.1016/j.mtchem.2023.101641
2468-5194/

the photocatalytic capability. Xu et al. synthesized TiO_2/Bi_2O_3 composite film by a sol-gel method and proved that the sample had good photocatalytic efficiency for X–3B [14]. Porous Bi_2O_3/Ti^{3+}-TiO_2 synthesized by hydrothermal method and photo-reduction exhibited great photocatalytic degradation capability for tetracycline hydrochloride (TCH) [15], and flower-like TiO_2/Bi_2O_3 prepared by hydrothermal and calcination methods provided satisfactory photocatalytic degradation efficiency for p-chlorophenol [16]. Huang et al. synthesized three-dimensional TiO_2/Bi_2O_3 hierarchical composites that showed good photocatalytic capability for methylene blue (MB). Although enhanced photocatalytic capability is obtained by the above-mentioned work, there are still some problems, such as low concentrations of pollutants adsorbed, irregular morphology, and tedious synthesis steps.

In this work, we successfully prepared TiO_2 nanotubes by sacrifice template, and then $Bi_2O_3/Bi_2O_{2.33}$ nanosheets were decorated on the TiO_2 nanotubes by the hydrothermal method. The formation of nanotubular structures endows $TiO_2/(Bi_2O_3/Bi_2O_{2.33})$ with a high specific area, and the heterostructure between TiO_2 and $Bi_2O_3/Bi_2O_{2.33}$ decelerates the recombination of photogenerated electron-hole pairs. The nonstoichiometric $Bi_2O_{2.33}$ provides more active sites for pollutant adsorption, all of which contribute to the efficient removal of organic pollutants.

2. Experimental

2.1. Materials

The main component of waste foam is polystyrene (PS), which is used as the starting material for the sacrifice template. Tetrabutyl titanate (TBOT, 97%), N, N-dimethylformamide (DMF, 99.5%), absolute ethanol, bismuth nitrate in glycol solution (volume ratio 1:10), methyl orange (MO), and rhodamine B (RhB) were purchased from Aladdin. TCH was purchased from McLean. All chemicals used in our experiments were of analytical grade and used without further purification.

2.2. Preparation of $TiO_2/(Bi_2O_3/Bi_2O_{2.33})$ heterostructure

The schematic preparation process of $TiO_2/(Bi_2O_3/Bi_2O_{2.33})$ is shown in Fig. 1. 1.4 g of waste foam was addedto 5 mL of DMF with magnetic stirring for 10 h at 60 °C. The obtained solution was loaded into a syringe connected to a 15.26 kV power source. The flow rate of the solution was controlled at 0.67 mL/h, and the distance from the needle to the rotating acceptor was 16 cm. The environmental humidity was maintained at 10%. A piece of PS fiber membrane was finally obtained through this process, which acted as a sacrificial template for preparing TiO_2 nanotubes. The membrane was then soaked in TBOT/ethanol (volume ratio: 1:10) precursor solution for 5 min, followed by drying treatment at 60 °C for 2 h. Next, the as-prepared sample was calcined in a tube furnace under an atmospheric environment at 550 °C for 1 h to remove the PS template. Finally, the TiO_2 nanotubes were obtained.

We put 0.03 g, 0.05 g, or 0.07 g of TiO_2 nanotube, 4 mL of 8 mmol/L bismuth nitrate solution, and 8 mL of absolute ethanol into a Teflon bladder, and then the mixture was sealed into a stainless-steel reaction kettle. The kettle was placed in a baking oven at 160 °C for 5 h. After the reaction, the products were washed with absolute ethanol three times and dried at 60 °C for 2 h. Thus, the TiO_2 nanotubes decorated with $Bi_2O_3/Bi_2O_{2.33}$ nanosheets were obtained, named TB1, TB2, and TB3, respectively.

2.3. Characterization

The morphological characterization was performed by scanning electron microscopy (SEM Helios G4 UC, Thermo Fisher Scientific). Characterization information on the phases and purity of samples was obtained by X-ray powder diffraction (XRD, SmartLab-9kW diffractometer, Rigaku) measured by using Cu Kα radiation ($\lambda = 0.15418$ nm) under 40 kV within a scanning range from 10° to 80°. The elemental composition of $TiO_2/(Bi_2O_3/Bi_2O_{2.33})$ nanotubes was determined by X-ray energy dispersive analysis (EDX, Aztec Live ULTIM, Oxford Instruments). The transmission electron microscope (TEM, Tecnai G^2 F20 S-TWIN, FEI Company) was used to obtain the exposed crystallographic plane of TiO_2 and bismuth oxide. The X-ray photoelectron spectroscopy (XPS) was carried out on the AXIS Ultra DLD. The UV–Vis diffuse reflectance spectra were measured by a fluorescence spectrometer (F-7000, Hitachi). The Mott-Schottky curve was monitored using an electrochemical workstation (CHI660E, Shanghai Chenhua). The degradation capability was determined by using UV–Vis spectrophotometry (UV-2550, Shimadzu) through measuring the absorbance of methyl orange (MO), rhodamine B (RhB), and tetracycline hydrochloride (TCH) at 450 nm, 546 nm, and 357 nm, respectively. A Hitachi F7000 fluorescence spectrophotometer was used for the photoluminescence (PL) measurements with an excitation of 325 nm. A Bruker EMX Plus spectrometer was used for the electron spin resonance (ESR) test to identify active species generated in the photocatalytic process.

2.4. Adsorption experiments

MO was used to indicate the adsorption capability of samples. At first, an aqueous solution of 20 mL MO with different concentrations of 50, 100, 150, 200, 300, and 400 mg/L) was prepared, and 20 mg samples were added to each MO solution. Then the mixture was stirred in dark conditions at room temperature for 24 h to reach the balance between adsorption and desorption. Afterward, the mixture was centrifuged to remove the photocatalyst. Several milliliters of MO solution were drawn at 30-min intervals to investigate the variation of pollutant concentration calculated from the UV–Vis spectrum. The adsorption capability of samples was

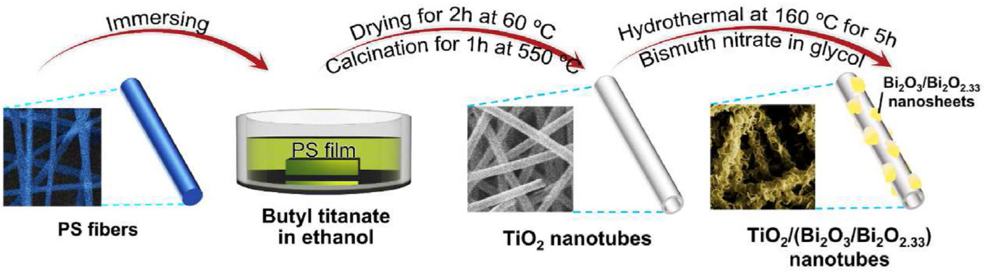

Fig. 1. Schematic preparation process for $TiO_2/(Bi_2O_3/Bi_2O_{2.33})$ nanotubes.

determined by the change in MO concentration. The pseudo-first-order and second-order kinetics were investigated by the MO concentration, which varied with time via mixing 20 mL MO (100 mg/L) with a 20 mg sample.

2.5. Photocatalytic experiments

The degradation of RhB was used as an indication to evaluate the photocatalytic activity of catalysts by measuring the concentration at a given time interval. At first, an aqueous solution of 20 mL of RhB (10 mg/L) was prepared, and photocatalysts (20 mg) were addedto the solution. Then the mixture was stirred under dark conditions for 20 min to reach the balance between adsorption and desorption. After that, the solution was irradiated under a xenon lamp (300 W) with stirring to ensure catalysts close contact with RhB. 1 mL of solution was drawn at a given time interval, separated by centrifuging, and then measured by UV–Vis spectrophotometry. Furthermore, we used TCH to evaluate the degradation capability of the photocatalysts against antibiotics. An aqueous solution of TCH (50 mg/L) was prepared. Then 20 mg of pure TiO_2 nanotubes, TB1, TB2, or TB3 were mixed with 20 mL of TCH solution at room temperature. After stirring for 40 min to reach adsorption and desorption equilibrium, the mixture was irradiated by a xenon lamp. The TCH degradation test was the same as that for RhB.

An electrochemical workstation with a three-electrode system was used to measure the transient photocurrent responses of TiO_2 nanotubes and $TiO_2/(Bi_2O_3/Bi_2O_{2.33})$ nanotubes under xenon lamp irradiation. First, 10 mg of photocatalysts were dispersed in 10 mL of C_2H_5OH, and then ITO conductive glass (1 cm^2) was dipped in the turbid liquid 40 times and dried at 200 °C for 1h to form the working electrode. The Pt and Ag/AgCl electrodes were used as reference and counter electrodes.

The reusability of $TiO_2/(Bi_2O_3/Bi_2O_{2.33})$ nanotubes was evaluated by the degradation of RhB. After each degradation loop, the photocatalysts were separated by centrifugation. The active agent species were analysed by adding scavengers EDTA-2Na, P-BQ, and TBA to capture photogenerated h^+, $\cdot O_2^-$, and $\cdot OH$ in reaction, respectively.

3. Results and discussion

The morphology images by SEM and TEM in Fig. 2a and Fig. S1b show TiO_2 nanotubes made from sacrificial template PS nanofibers (Fig. S1a). TiO_2 nanotubes are uniform in morphology, with a smooth surface and a diameter of about 950 nm. The hollow structure can be observed clearly in Fig. S1b. The morphology of samples TB1, TB2, and TB3 is presented in Fig. 2b–d. It can be seen that nanosheets successfully grow on the TiO_2 nanotubes, and the growing density of nanosheets decreases with the amount of TiO_2 nanotubes increasing from TB1 to TB3. Moreover, the nanosheets are homogeneously spread on the TiO_2 nanotubes' surface without any aggregation, which is conducive to the increase of specific surface area and the exposure of active sites. The EDX analysis and elemental mapping of the TB2 sample are shown in Fig. S1c and Fig. S2, respectively. It can be clearly seen that Ti, O, and Bi elements are evenly distributed on nanotubes. As shown in the TEM image of TB2 in Fig. 2e, the morphology of nanosheets grown on nanotubes can be easily observed. The high-resolution TEM (HRTEM) image of TB2 can be found in Fig. 2f. Three groups of lattice fringes show an interplanar distance of 0.346 nm, 0.328 nm, and 0.270 nm, corresponding to the (101) plane of anatase TiO_2, (201) plane of β-Bi_2O_3, and (110) plane of $Bi_2O_{2.33}$, respectively. This result implies that the nanosheets are composed of β-Bi_2O_3 and $Bi_2O_{2.33}$, and the $TiO_2/(Bi_2O_3/Bi_2O_{2.33})$ heterojunction is successfully formed.

XRD measurements are carried out to further determine the crystal structure of samples. As shown by XRD patterns in Fig. 3a, the diffraction peaks of TiO_2 nanotubes can be indexed to the TiO_2 anatase structure (JCPDS 21–1272), which has been demonstrated to be beneficial to the photocatalytic degradation of organic pollutants [17]. As for the samples TB1, TB2, and TB3, in addition to the diffraction peaks ascribed to anatase TiO_2, the characteristic peak at about 27.95° can be assigned to the (201) plane of β-Bi_2O_3 (JCPDS 27–0050), and the peaks at about 32.88° and 47.16° can be indexed to the (110) and (200) planes of $Bi_2O_{2.33}$ (JCPDS 27–0051), respectively. That is to say, β-Bi_2O_3 and nonstoichiometric $Bi_2O_{2.33}$ with more oxygen vacancies simultaneously exist in these samples except for anatase TiO_2, where the former component is conducive to the photocatalytic degradation [18], and the latter contributes to

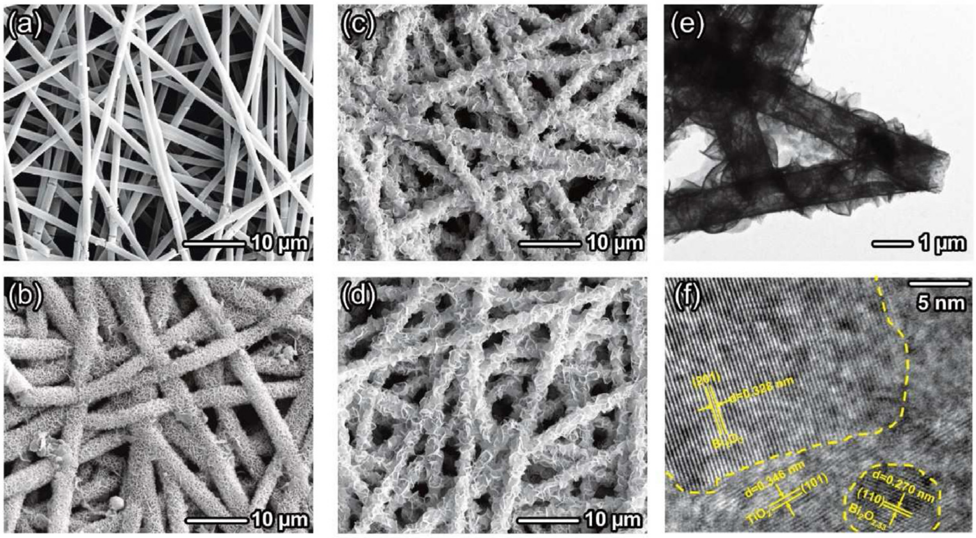

Fig. 2. SEM images of samples: (a) TiO_2 nanotubes, (b) TB1 nanotubes, (c) TB2 nanotubes, and (d) TB3 nanotubes. TEM (e) and HRTEM (f) images of TB2 nanotubes.

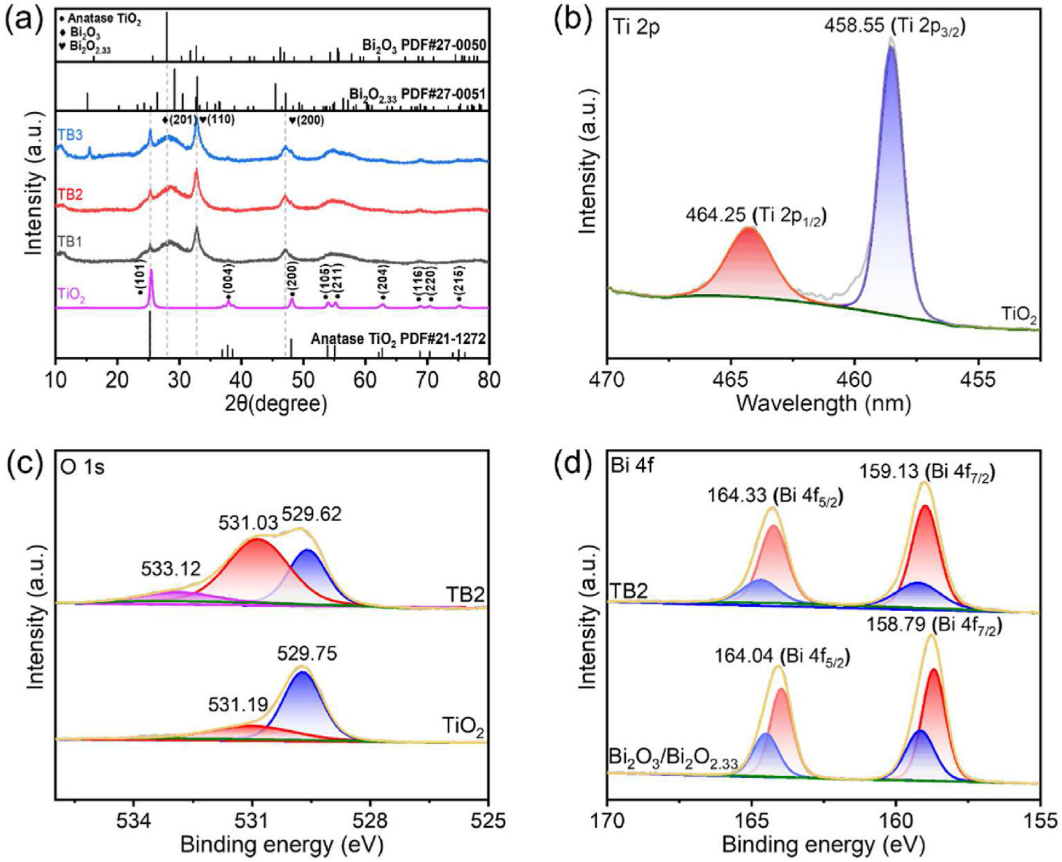

Fig. 3. (a) XRD patterns of the samples TB1, TB2, TB3, and TiO_2 nanotubes. High-resolution XPS spectra of (b) Ti 2p for TiO_2 samples, (c) O 1s for TiO_2 and TB2 samples, and (d) Bi 4f for $Bi_2O_3/Bi_2O_{2.33}$ and TB2 samples.

the enhanced adsorption capacity [13]. Furthermore, with the amount of TiO_2 nanotubes increasing from TB1 to TB3, the diffraction peak at about 25.28° strengthens, which corresponds to the (101) plane of anatase TiO_2, indicating a reduction trend in $Bi_2O_3/Bi_2O_{2.33}$ loading.

The XPS tests are conducted to determine the samples' chemical composition and binding energy. The full XPS spectra calibrated by the C 1s peak (284.6 eV) for TiO_2 nanotubes and TB2 are shown in Fig. S3. In addition to the Ti 2p peak, Bi 4f can be observed for the TB2 sample, suggesting the successful loading of bismuth oxide on the TiO_2 nanotube. As shown in the high-resolution XPS spectrum of Ti 2p for the TiO_2 sample in Fig. 3b, two characteristic peaks located at 458.55 eV and 464.25 eV can be ascribed to Ti $2p_{3/2}$ and Ti $2p_{1/2}$, respectively. The splitting energy between these two peaks is 5.7 eV, suggesting a Ti^{4+} oxidation state in TiO_2 nanotubes [19–22]. The high-resolution XPS spectra of O1s are shown in Fig. 3c. In addition to one additional peak at 533.12 eV assigned to surface hydroxyl groups for the TB2 sample, the spectra of O 1s for TiO_2 and TB2 are fitted into two main peaks. The peaks at higher and lower energy are ascribed to the oxygen vacancy and the lattice oxygen, respectively. The large peak area centered at 531.03 eV for TB2 reveals the high content of oxygen vacancy with the existence of $Bi_2O_{2.33}$. In the high-resolution XPS spectrum of Bi 4f in Fig. 3d for TB2, two peaks with a binding energy of 164.33 eV and 159.13 eV are indexed to Bi $4f_{5/2}$ and Bi $4f_{7/2}$, respectively. Compared with the $Bi_2O_3/Bi_2O_{2.33}$ sample, these two peaks shift to higher binding energy, which implies that the electrons flow from Bi_2O_3 to TiO_2. Furthermore, Bi $4f_{5/2}$ or Bi $4f_{7/2}$ peak can be divided into two spin-orbit components corresponding to Bi^{3+} at higher binding energy and Bi^{2+} at lower binding energies, respectively.

The UV–Vis diffuse reflectance spectra were carried out to investigate the light absorption of samples. As we can see in Fig. 4a, in the range of 380–700 nm, the light absorption of TB1, TB2, and TB3 is higher than that of pure TiO_2 nanotubes, suggesting enhanced visible light capture ability. The higher absorption rate is due to the interaction between TiO_2 and $Bi_2O_3/Bi_2O_{2.33}$ [23]. The samples' bandgap values in Fig. 4b were evaluated by the Tauc plot. The calculation formula is shown [24]:

$$(Ah\nu)^{1/n} = B(h\nu - E_g) \tag{1}$$

where A is the absorbance of samples, h is the Planck constant, ν is incident photon frequency, E_g is the bandgap, and B is a proportional constant. As shown in Fig. 4b, the bandgaps of TB1, TB2, and TB3 samples are significantly smaller than those of pure TiO_2, which endows them with stronger visible light absorption and photocatalytic ability. The bandgap of TiO_2 is smaller than the theoretical value, which may result from the titanium-terminated anatase surface with a reduced bandgap [25].

The Mott-Schottky test was carried out to investigate the type of semiconductor and position of flat potential (E_{fp}) which can help orientate the samples' band position [26,27]. As we can see in Fig. 4c and d, the curve slopes of samples TB1, TB2, TB3, TiO_2, and $Bi_2O_3/Bi_2O_{2.33}$ are positive, suggesting all the samples are n-type semiconductors [28]. The E_{fp} (vs. Ag/AgCl) of TB1, TB2, TB3, TiO_2, and $Bi_2O_3/Bi_2O_{2.33}$ are −0.179 eV, −0.256 eV, −0.018 eV, −0.611 eV,

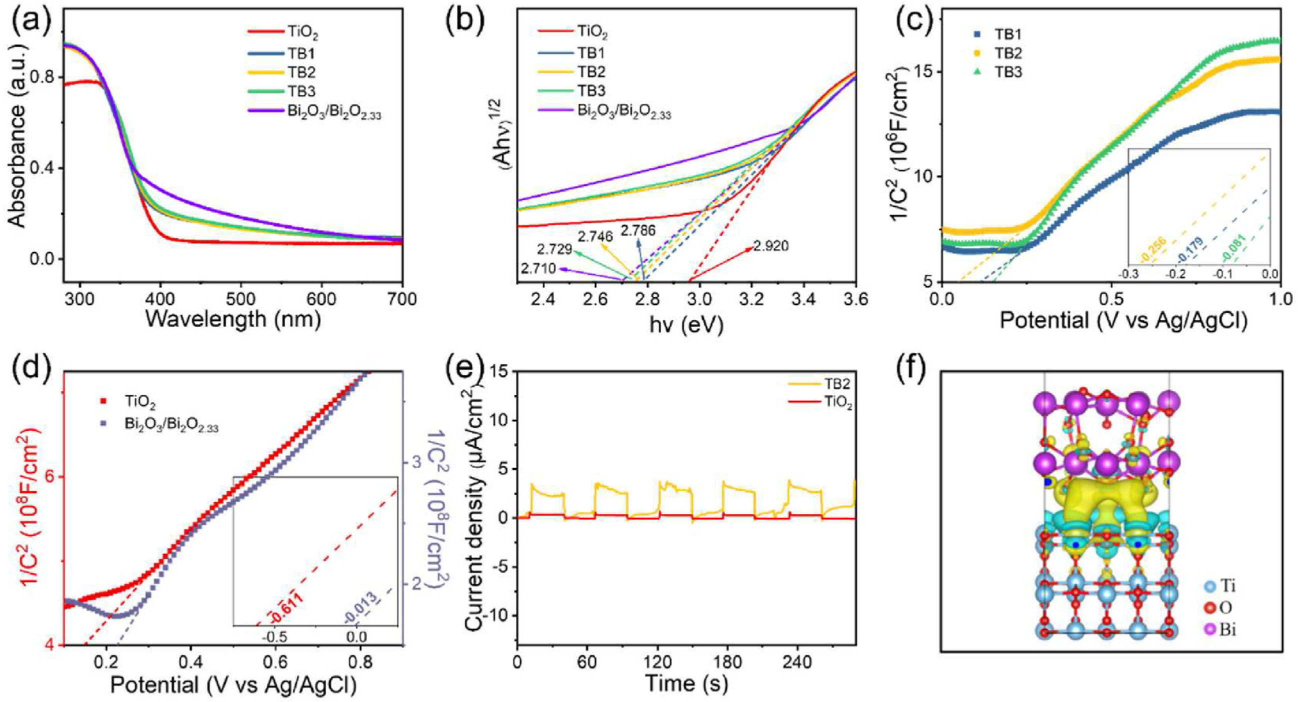

Fig. 4. (a) UV−Vis diffuse reflectance spectra, (b) estimated bandgap of samples by Tauc plots, (c) and (d) Mott-Schottky plots, and (e) transient photocurrent responses of samples. (f) Differential charge density of TiO_2/Bi_2O_3 from the front view.

and −0.013 eV, respectively, which can be transformed to potential (vs. NHE) by the equation [29,30]:

$$E_{NHE} = E_{fp} + E^0_{Ag/AgCl} \tag{2}$$

where $E^0_{Ag/AgCl}$ = 0.210 eV [31]. So, the E_{NHE} of TiO_2 and $Bi_2O_3/Bi_2O_{2.33}$ can be calculated to be about −0.401 eV and 0.197 eV, respectively. Many studies have shown that the conduction band minimum (CBM) of n-type semiconductors is about 0.1 eV more negative than E_{fp} [32]. Thus, the CBM of TiO_2 and $Bi_2O_3/Bi_2O_{2.33}$ is evaluated to be −0.501 eV and 0.097 eV (vs. NHE), respectively. Based on a previous calculation, the valence band maximum (VBM) of TiO_2 and $Bi_2O_3/Bi_2O_{2.33}$ can be about 2.419 eV and 2.807 eV, respectively.

The transient photocurrent responses were recorded to investigate the sample's light response. As can be seen from Fig. 4e and Fig. S4, the current density of TB2 is the strongest. Although the photocurrent value is not significant compared to other reports, as shown in Table S1, it is about 7 times higher than that of TiO_2, revealing the stronger charge separation capability of TB2 compared to pure TiO_2. The PL spectra of samples are shown in Fig. S5. The fluorescence intensity of TB2 is smaller than that of pure TiO_2 nanotubes, which further indicates that the heterostructure elongates the lifetime of photo-induced electron-hole pairs.

To investigate the interaction between the components of the heterostructure, the theoretical calculation was carried out using the exchange−correlation functional PBE through the Vienna ab-initio simulation package (VASP) and projector augmented wave method [33,34]. Since the valance band energy of $Bi_2O_{2.33}$ is insufficient to produce active radical •OH [35], the $TiO_2/(Bi_2O_3/Bi_2O_{2.33})$ heterostructure is simplified to the TiO_2/Bi_2O_3 heterojunction. All the models used in the calculation are based on experimentally determined lattice parameters [36,37]. The plane wave cutoff energy is set at 420 eV and a G-centered 3 × 4 × 1 *k*-point mesh. As can be seen in Fig. S6, the calculated bandgap of TiO_2/Bi_2O_3 is 1.45 eV, which is much smaller than the theoretical bandgap of anatase TiO_2 [38], suggesting the interaction of TiO_2 and Bi_2O_3 decreases the bandgap. The calculated value is in line with the reduced bandgap measured by UV−Vis diffuse reflectance, indicating a stronger light adsorption capability. The differential charge density of TiO_2/Bi_2O_3 nanostructures is shown in Fig. 4f and Fig. S7. The light-blue part between TiO_2 and Bi_2O_3 means depletion of electrons, and the light-yellow part means accumulation of electrons. The light-blue and light-yellow parts are well separated, suggesting a good charge separation capability [39].

To investigate the adsorption and photocatalytic performance, the adsorption of MO and the degradation of RhB and TCH under a 300 W xenon lamp were carried out. As shown in Fig. 5a, samples TB1, TB2, and TB3 are used to adsorb 100 mg/L MO. MO is a cationic dye [40], which can generate positive ions when dissolving in water, while the O atom in bismuth oxide has strong electronegativity [41]. Thus, the Coulomb force can be generated between positive ions and O atoms, which strengthens the samples' adsorption capability. Also, oxygen vacancies in $Bi_2O_{2.33}$ will help improve the adsorption capability [13]. As we see from Fig. 5a, TB2 can reach 70 mg/g adsorption within 1 h, which is larger than samples TB1 and TB3. Higher or lower $Bi_2O_3/Bi_2O_{2.33}$ nanosheet loads on TiO_2 nanotubes do not enhance adsorption. The pseudo-first-order and pseudo-second-order adsorption kinetics are analyzed by the following equations:

$$\ln(q_e - q_t) = \ln q_e - k_1 t \tag{3}$$

$$1/(q_e - q_t) = 1/q_e + k_2 t \tag{4}$$

where q_e and q_t (mg/g) mean the adsorption capacities under equilibrium state and at time t (min), respectively, and k_1 and k_2 mean the pseudo-first-order kinetic rate constant and pseudo-second-order kinetic rate constant, respectively. As shown in Fig. 5b, the correlation coefficient (R^2) of pseudo-first-order

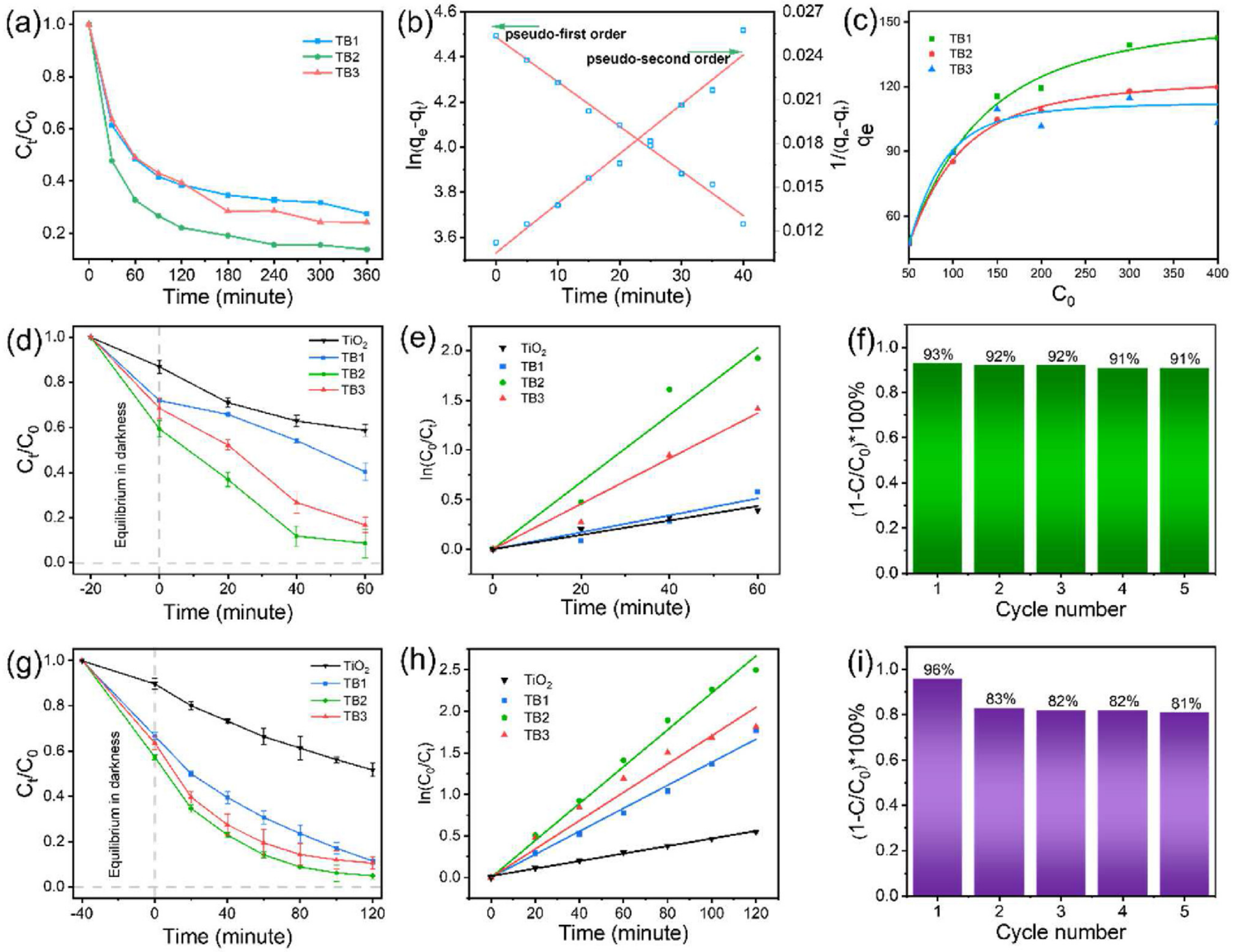

Fig. 5. (a) MO adsorption over TB1, TB2, and TB3, (b) Pseudo-first-order kinetics and Pseudo-second-order kinetics curves of MO over TB2, (c) Adsorption isotherms of MO on TB1, TB2, and TB3 (t = 24 h), (d) RhB (10 mg/L) removal over different photocatalysts, (e) Pseudo-first-order reaction kinetics curves of RhB removal, (f) RhB (10 mg/L) cycling degradation over TB2 photocatalyst, (g) TCH (50 mg/L) removal over different photocatalysts, (h) Pseudo-first-order reaction kinetics curves of TCH removal, (i) TCH (50 mg/L) cycling degradation over TB2 photocatalyst.

kinetics ($R^2 = 0.9913$) is higher than that of pseudo-second-order kinetics ($R^2 = 0.9681$), indicating that internal diffusion is the rate-determining step. As we can see from Fig. 5c, with an increase in $Bi_2O_3/Bi_2O_{2.33}$ load on TiO_2 from TB3 to TB1, the maximum MO adsorption capacity gradually increases.

The Langmuir isotherm model is used to analyze the adsorption process using the following equation:

$$C_e / q_e = C_e / q_m + 1 / (K_L * q_m) \tag{5}$$

where q_e (mg/g) and C_e (mg/L) mean adsorption capacity and concentration of solution under equilibrium state, respectively, K_L is the Langmuir isothermal constant, and q_m (mg/g) presents the maximum adsorption capacity.

The degradation of 10 mg/L RhB is shown in Fig. 5d. As we can see from Fig.s. 5d and 93%, RhB is removed by TB2 after 1 h of irradiation. In order to reveal the photocatalytic activity, the degradation kinetics of RhB are linearly fitted, as shown in Fig. 5e. The degradation activity of TB2 is 4.66-fold higher than that of TiO_2. The outstanding RhB degradation efficiency results from the interaction between TiO_2 and $Bi_2O_3/Bi_2O_{2.33}$, which narrows the bandgap compared with TiO_2 (shown in Fig. 4b) and enhances the capability of charge separation (shown in Figs. 4e and f). In addition, the more active sites introduced by $Bi_2O_3/Bi_2O_{2.33}$ also contribute to the high performance. To investigate the reusability of TB2, cycling degradation of RhB (10 mg/L) is carried out. After one cycle of RhB degradation, the sample was washed with deionized water and dried overnight at 60 °C. As shown in Fig. 5f, even after five cycles of RhB degradation, the removal rate is still as high as 91%, which reveals the excellent reusability and stability of TB2. A degradation experiment was conducted using 50 mg/L TCH to demonstrate its practical use. In Fig. 5g, the TCH removal over TB2 reached 96% after 120 min of irradiation. The degradation kinetics of TCH are linearly fitted, as shown in Fig. 5h. The degradation activity of TB2 is 4.92-fold higher than that of TiO_2, suggesting great photocatalytic activity in the $TiO_2/(Bi_2O_3/Bi_2O_{2.33})$ compound. The cycling degradation of TCH is shown in Fig. 5i; it can be seen that the removal rate of TCH still remains at 81% after five cycles. The XRD patterns of the TB2 photocatalyst before and after successive testing are shown in Fig. S8. There is no obvious difference in their characteristic peaks, which means satisfactory stability for TB2. The decrease in degradation rate between the first and second cycles can result from the destruction of nanotubes, which will impede the adsorption rate. Then, the degradation rate becomes stable after further cycling.

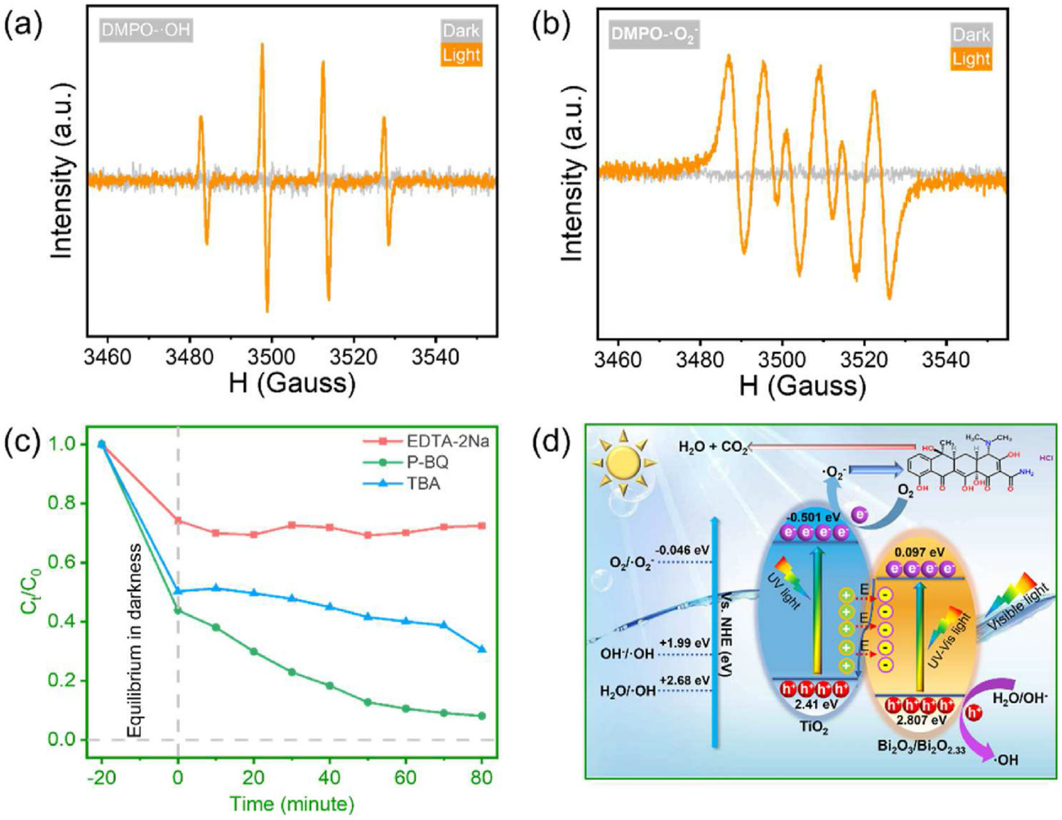

Fig. 6. ESR spin-tripping spectra for (a) DMPO-•OH and (b) DMPO-•O_2^- using TB2, (c) trapping experiments in photocatalytic degradation of RhB (10 mg/L) over TB2, (d) The illustration of RhB photocatalytic degradation by TiO_2/(Bi_2O_3/$Bi_2O_{2.33}$) photocatalyst under full-spectrum light irradiation.

To elucidate the mechanism behind photocatalytic degradation, trapping experiments were carried out to find the main oxide species, and an ESR test was employed to identify the active species in the photocatalytic process [42–47] of TB2 by using 5,5-dimethyllpyrroline N-oxide (DMPO) as the spin-trapping agent. As shown in Fig. 6a, no DMPO-•OH signal is detected in the dark, while the characteristic 1:2:2:1 quadruple peak of DMPO-•OH is observed under illumination, indicating the generation of hydroxyl radicals in the solution under light irradiation with TB2. As shown in Fig. 6b, no DMPO-•O_2^- signal is detected in the dark, while the characteristic peak of DMPO-•O_2^- is detected under illumination, indicating that the photogenerated electrons in TB2 reduce dissolved oxygen to generate superoxide anion radicals. ESR analysis confirms the generation of •OH and •O_2^- during the photocatalytic process of TB2. The trapping experiment results are shown in Fig. 6c. Three trapping agents, TBA, EDTA-2Na, and P-BQ, can capture the active radicals •OH, h^+, and •O_2^-, respectively [15,48,49]. As shown in Fig. 6c, with the addition of EDTA-2Na, the efficiency of RhB degradation shows a great decline compared with the result shown in Fig. 5d, indicating that h^+ plays a key role in the photocatalytic degradation. The •OH radical also plays a more important role since the degradation is hindered by the addition of TBA. The standard redox potentials (O_2/•O_2^-, H_2O/•OH and OH^-/•OH) [50,51] and band structures of TiO_2 and Bi_2O_3/$Bi_2O_{2.33}$ are shown in Fig. 6d. According to the band position calculated from Mott-Schottky measurements, the contact of Bi_2O_3/$Bi_2O_{2.33}$ and TiO_2 forms an S-scheme heterostructure. At the beginning of contact, the electron in the conduction band (CB) of TiO_2 flows into Bi_2O_3/$Bi_2O_{2.33}$ driven by the built-in potential difference. Then, accumulation of electrons appears on the Bi_2O_3/$Bi_2O_{2.33}$ side, while electron depletion appears on the TiO_2 side, respectively, near the interface, which will generate an internal electric field from TiO_2 to Bi_2O_3/$Bi_2O_{2.33}$. Photogenerated carriers occur in the heterostructure under light irradiation. The internal electric field promotes the flow of photogenerated electrons from the CB of Bi_2O_3/$Bi_2O_{2.33}$ to TiO_2, which recombine with holes in the VB of TiO_2. Thus, the electrons in CB of TiO_2 and holes in VB of Bi_2O_3/$Bi_2O_{2.33}$ will be retained in their own positions, which possess great redox ability. Therefore, the h^+ in Bi_2O_3/$Bi_2O_{2.33}$ will react with H_2O or OH^- to produce •OH radicals, and the h^+ also directly participates in RhB photocatalytic degradation, which endows TiO_2/(Bi_2O_3/$Bi_2O_{2.33}$) high photocatalytic performance.

4. Conclusions

This work proposes a facile avenue to prepare TiO_2/(Bi_2O_3/$Bi_2O_{2.33}$) catalysts using sacrificial templates and a hydrothermal process. The heterojunction between TiO_2 and Bi_2O_3/$Bi_2O_{2.33}$ narrows the bandgap to 2.746 eV and retains the electrons in CB of TiO_2 and holes in VB of Bi_2O_3/$Bi_2O_{2.33}$, which possess great redox capability. The TB2 could remove 93% of RhB (10 mg/L) within 60 min and 96% of TCH (50 mg/L) within 120 min, respectively. Meanwhile, combining TiO_2 and Bi_2O_3/$Bi_2O_{2.33}$ endows the catalyst with great adsorption capability, removing 70% of MO (100 mg/L) within 60 min. The photocatalyst's recyclability was confirmed through repeated degradation experiments. This work provides a facile approach to synthesizing nanotubular S-scheme heterojunction photocatalysts with great photocatalytic and adsorption performance.

CRediT author statement

Ran Lu: Writing - Original Draft, Validation, Formal analysis, Visualization, Software, Methodology;

Sheng-Zhe Zhao: Formal analysis, Validation;
Yi Yang: Visualization, Validation;
Yan Wang: Resources;
Hong-Lan Huang: Resources;
Yong-Da Hu: Resources;
Raul D. Rodriguez: Writing - Review & Editing;
Jin-Ju Chen: Conceptualization, Supervision.

Declaration of competing interest

The authors declare that they have no known competing financial interests or personal relationships, that could have appeared to influence the work reported in this paper.

Data availability

The data that has been used is confidential.

Acknowledgements

The work was supported by the Sichuan Science and Technology Program (grant No 2023YFG0215). RDR thanks support by RFBR, project number 21-53-12045.

Appendix A. Supplementary data

Supplementary data to this article can be found online at https://doi.org/10.1016/j.mtchem.2023.101641.

References

[1] F. Ding, M.L. Gao, Pore wettability for enhanced oil recovery, contaminant adsorption and oil/water separation, Adv. Colloid Interface Sci. 289 (2021) 24, https://doi.org/10.1016/j.cis.2021.102377.

[2] T. Ohno, S.Y. Lee, Y. Yang, Fabrication of morphology-controlled TiO_2 photocatalyst nanoparticles and improvement of photocatalytic activities by modification of Fe compounds, Rare Met. 34 (2015) 291–300, https://doi.org/10.1007/s12598-015-0483-8.

[3] M. Zhu, L.S. Zhang, S.S. Liu, D.K. Wang, Y.C. Qin, Y. Chen, W.L. Dai, Y.H. Wang, Q.J. Xing, J.P. Zou, Degradation of 4-nitrophenol by electrocatalysis and advanced oxidation processes using Co_3O_4@C anode coupled with simultaneous CO_2 reduction via SnO_2/CC cathode, Chin. Chem. Lett. 31 (2020) 1961–1965, https://doi.org/10.1016/j.cclet.2020.01.017.

[4] M.M. Luan, G.L. Jing, Y.J. Piao, D.B. Liu, L.F. Jin, Treatment of refractory organic pollutants in industrial wastewater by wet air oxidation, Arab. J. Chem. 10 (2017) S769–S776, https://doi.org/10.1016/j.arabjc.2012.12.003.

[5] S. Cheng, S.D. Zhao, B.L. Xing, Y.Z. Liu, C.X. Zhang, H.Y. Xia, Preparation of magnetic adsorbent-photocatalyst composites for dye removal by synergistic effect of adsorption and photocatalysis, J. Clean. Prod. 348 (2022) 11, https://doi.org/10.1016/j.jclepro.2022.131301.

[6] H. Nishikiori, S. Fujiwara, S. Miyagawa, N. Zettsu, K. Teshima, Crystal growth of titania by photocatalytic reaction, Appl. Catal. B Environ. 217 (2017) 241–246, https://doi.org/10.1016/j.apcatb.2017.05.076.

[7] M. Kapilashrami, Y.F. Zhang, Y.S. Liu, A. Hagfeldt, J.H. Guo, Probing the optical property and electronic structure of TiO_2 nanomaterials for renewable energy applications, Chem. Rev. 114 (2014) 9662–9707, https://doi.org/10.1021/cr5000893.

[8] A. Biswas, A. Chakraborty, N.R. Jana, Nitrogen and fluorine codoped, colloidal TiO_2 nanoparticle: tunable doping, large red-shifted band edge, visible light induced photocatalysis, ACS Appl. Mater. Interfaces 10 (2018) 1976–1986, https://doi.org/10.1021/acsami.7b14025.

[9] J.Z. Huang, K. Fu, X.L. Deng, N.N. Yao, M.Z. Wei, Fabrication of TiO_2 nanosheet arrays/graphene/Cu_2O composite structure for enhanced photocatalytic activities, Nanoscale Res. Lett. 12 (2017) 6, https://doi.org/10.1186/s11671-017-2088-7.

[10] X.L. Hu, Y.Y. Li, J. Tian, H.R. Yang, H.Z. Cui, Highly efficient full solar spectrum (UV-vis-NIR) photocatalytic performance of Ag_2S quantum dot/TiO_2 nanobelt heterostructures, J. Ind. Eng. Chem. 45 (2017) 189–196, https://doi.org/10.1016/j.jiec.2016.09.022.

[11] Y. Cheng, J.Z. Gao, Q.W. Shi, Z.C. Li, W.X. Huang, In situ electrochemical reduced Au loaded black TiO_2 nanotubes for visible light photocatalysis, J. Alloys Compd. 901 (2022) 9, https://doi.org/10.1016/j.jallcom.2021.163562.

[12] H.J. Lu, Q. Hao, T. Chen, L.H. Zhang, D.M. Chen, C. Ma, W.Q. Yao, Y.F. Zhu, A high-performance Bi_2O_3/Bi_2SiO_5 p-n heterojunction photocatalyst induced by phase transition of Bi_2O_3, Appl. Catal. B Environ. 237 (2018) 59–67, https://doi.org/10.1016/j.apcatb.2018.05.069.

[13] S.W. Liu, S.H. Kang, H.M. Wang, G.Z. Wang, H.J. Zhao, W.P. Cai, anosheets-built flowerlike micro/nanostructured $Bi_2O_{2.33}$ and its highly efficient iodine removal performances, Chem. Eng. J. 289 (2016) 219–230, https://doi.org/10.1016/j.cej.2015.12.101.

[14] J. Xu, Y. Ao, D. Fu, C. Yuan, Synthesis of Bi_2O_3–TiO_2 composite film with high-photocatalytic activity under sunlight irradiation, Appl. Surf. Sci. 255 (2008) 2365–2369, https://doi.org/10.1016/j.apsusc.2008.07.095.

[15] T. Tang, Z. Yin, J. Chen, S. Zhang, W. Sheng, W. Wei, Y. Xiao, Q. Shi, S. Cao, Novel p-n heterojunction Bi_2O_3/Ti^{3+}-TiO_2 photocatalyst enables the complete removal of tetracyclines under visible light, Chem. Eng. J. 417 (2021), https://doi.org/10.1016/j.cej.2020.128058.

[16] J.A. Zhu, S.H. Wang, J.U. Wang, D.Q. Zhang, H.X. Li, Highly active and durable Bi_2O_3/TiO_2 visible photocatalyst in flower-like spheres with surface-enriched Bi_2O_3 quantum dots, Appl. Catal. B Environ. 102 (2011) 120–125, https://doi.org/10.1016/j.apcatb.2010.11.032.

[17] C. Dette, M.A. Perez-Osorio, C.S. Kley, P. Punke, C.E. Patrick, P. Jacobson, F. Giustino, S.J. Jung, K. Kern, TiO_2 anatase with a bandgap in the visible region, Nano Lett. 14 (2014) 6533–6538, https://doi.org/10.1021/nl503131s.

[18] S. Wu, Y. Zhao, X.X. Deng, X.L. Yang, X.Y. Wang, Y.Q. Zhao, Oxygen defects engineered CdS/$Bi_2O_{2.33}$ direct Z-Scheme heterojunction for highly sensitive photoelectrochemical assay of Hg^{2+}, Talanta 217 (2020) 9, https://doi.org/10.1016/j.talanta.2020.121090.

[19] S. Tan, Z. Xing, J. Zhang, Z. Li, X. Wu, J. Cui, J. Kuang, Q. Zhu, W. Zhou, Ti^{3+}-TiO_2/g-C_3N_4 mesostructured nanosheets heterojunctions as efficient visible-light-driven photocatalysts, J. Catal. 357 (2018) 90–99, https://doi.org/10.1016/j.jcat.2017.08.006.

[20] X. Zheng, D. Li, X. Li, J. Chen, C. Cao, J. Fang, J. Wang, Y. He, Y. Zheng, Construction of ZnO/TiO_2 photonic crystal heterostructures for enhanced photocatalytic properties, Appl. Catal. B Environ. 168–169 (2015) 408–415, https://doi.org/10.1016/j.apcatb.2015.01.001.

[21] V. Bilovol, S. Ferrari, D. Derewnicka, F.D. Saccone, XANES and XPS study of electronic structure of Ti-enriched Nd–Fe–B ribbons, Mater. Chem. Phys. 146 (2014) 269–276, https://doi.org/10.1016/j.matchemphys.2014.03.021.

[22] M.H. Basha, N.O. Gopal, Solution combustion synthesis and characterization of phosphorus doped TiO_2-CeO_2 nanocomposite for photocatalytic applications, Mater. Sci. Eng. B-Adv. Funct. Solid-State Mater. 236 (2018) 43–47, https://doi.org/10.1016/j.mseb.2018.12.001.

[23] M.N. Gómez-Cerezo, M.J. Muñoz-Batista, D. Tudela, M. Fernández-García, A. Kubacka, Composite Bi_2O_3–TiO_2 catalysts for toluene photo-degradation: ultraviolet and visible light performances, Appl. Catal. B Environ. 156–157 (2014) 307–313, https://doi.org/10.1016/j.apcatb.2014.03.024.

[24] J. Tauc, The Optical Propeties of Solids, 1972.

[25] C. Dette, M.A. Pérez-Osorio, C.S. Kley, P. Punke, C.E. Patrick, P. Jacobson, F. Giustino, S.J. Jung, K. Kern, TiO_2 anatase with a bandgap in the visible region, Nano Lett. 14 (11) (2014) 6533–6538, https://doi.org/10.1021/nl503131s.

[26] K. Gelderman, L. Lee, S.W. Donne, Flat-band potential of a semiconductor: using the Mott Schottky equation, J. Chem. Educ. 84 (2007) 685–688, https://doi.org/10.1021/ed084p685.

[27] N. Benreguia, S. Omeiri, B. Bellal, M. Trari, Visible light induced H_2PO_4-removal over $CuAlO_2$ catalyst, J. Hazard Mater. 192 (2011) 1395–1400, https://doi.org/10.1016/j.jhazmat.2011.06.049.

[28] H. Liu, D. Chen, Z. Wang, H. Jing, R. Zhang, Microwave-assisted molten-salt rapid synthesis of isotype triazine-/heptazine based g-C_3N_4 heterojunctions with highly enhanced photocatalytic hydrogen evolution performance, Appl. Catal. B Environ. 203 (2017) 300–313, https://doi.org/10.1016/j.apcatb.2016.10.014.

[29] J. Wang, Y. Yu, L. Zhang, Highly efficient photocatalytic removal of sodium pentachlorophenate with Bi_3O_4Br under visible light, Appl. Catal. B Environ. 136–137 (2013) 112–121, https://doi.org/10.1016/j.apcatb.2013.02.009.

[30] Y. Surendranath, D.A. Lutterman, Y. Liu, D.G. Nocera, Nucleation, growth, and repair of a cobalt-based oxygen evolving catalyst, J. Am. Chem. Soc. 134 (2012) 6326–6336, https://doi.org/10.1021/ja3000084.

[31] E. Friis, J. Andersen, L.L. Madsen, N. Bonander, P. Møller, J. Ulstrup, Dynamics of Pseudomonas aeruginosa azurin and its Cys3Ser mutant at single-crystal gold surfaces investigated by cyclic voltammetry and atomic force microscopy, Electrochim. Acta (1997), https://doi.org/10.1016/S0013-4686(98)99006-5.

[32] W. Liu, L. Qiao, A. Zhu, Y. Liu, J. Pan, Constructing 2D BiOCl/C_3N_4 layered composite with large contact surface for visible-light-driven photocatalytic degradation, Appl. Surf. Sci. 426 (2017) 897–905, https://doi.org/10.1016/j.apsusc.2017.07.225.

[33] G. Kresse, D. Joubert, From ultrasoft pseudopotentials to the projector augmented-wave method, Phys. Rev. B 59 (1999) 1758–1775, https://doi.org/10.1103/PhysRevB.59.1758.

[34] P.E. Blöchl, Projector augmented-wave method, Phys. Rev. B 50 (1994) 17953–17979, https://doi.org/10.1103/PhysRevB.50.17953.

[35] Y. Peng, K.K. Wang, T. Liu, J. Xu, B. Xu, Synthesis of one-dimensional Bi_2O_3-$Bi_2O_{2.33}$ heterojunctions with high interface quality for enhanced visible light photocatalysis in degradation of high-concentration phenol and MO dyes, Appl. Catal. B Environ. 203 (2017) 946–954, https://doi.org/10.1016/j.apcatb.2016.11.011.

[36] M. Horn, C.F. Schwebdtfeger, E.P. Meagher, Refinement of the structure of anatase at several temperatures, Z Krist-cryst. Mater. 136 (1972) 273–281, https://doi.org/10.1524/zkri.1972.136.16.273.

[37] C. Jovalekic, M. Zdujic, D. Poleti, L. Karanovic, M. Mitric, Structural and electrical properties of the 2Bi(2)O(3) center dot 3ZrO(2) system, J. Solid State Chem. 181 (2008) 1321–1329, https://doi.org/10.1016/j.jssc.2008.02.038.

[38] K. Persson, Materials Data on TiO_2 (SG: 141) by Materials Project, vol. 10, 2014 1207597, https://doi.org/10.17188/1207597. USA.

[39] R.J. Meng, Q.Y. Deng, C.X. Peng, B.J. Chen, K.X. Liao, L.J. Li, Z.Y. Yang, D.L. Yang, L. Zheng, C. Zhang, J.H. Yang, Two-dimensional organic-inorganic heterostructures of in situ-grown layered COF on Ti_3C_2 MXene nanosheets for lithium-sulfur batteries, Nano Today 35 (2020) 8, https://doi.org/10.1016/j.nantod.2020.100991.

[40] R. Yu, Y. Shi, D. Yang, Y. Liu, J. Qu, Z.-Z. Yu, Graphene oxide/chitosan aerogel microspheres with honeycomb-cobweb and radially oriented microchannel structures for broad-spectrum and rapid adsorption of water contaminants, ACS Appl. Mater. Interfaces 9 (2017) 21809–21819, https://doi.org/10.1021/acsami.7b04655.

[41] A.L. Allred, Electronegativity values from thermochemical data, J. Inorg. Nucl. Chem. 17 (1961) 215–221, https://doi.org/10.1016/0022-1902(61)80142-5.

[42] Q. Wang, Y. Zhao, Z. Zhang, S. Liao, Y. Deng, X. Wang, Q. Ye, K. Wang, Hydrothermal preparation of Sn_3O_4/TiO_2 nanotube arrays as effective photocatalysts for boosting photocatalytic dye degradation and hydrogen production, Ceram. Int. 49 (4) (2023) 5977–5985, https://doi.org/10.1016/j.ceramint.2022.11.113.

[43] K. Wang, Q. Wang, Y. Zhao, Z. Zhang, S. Liao, Y. Deng, X. Wang, Q. Ye, Hydrothermal synthesis of Z-scheme Bi_2WO_6/Bi_2MoO_6 heterojunctions for the enhanced photoelectrocatalytic performance of TiO2 NTs: structure, activity and mechanism approach, Fuel 339 (2023) 126973, https://doi.org/10.1016/j.fuel.2022.126973.

[44] Q. Wang, S. Zhu, S. Zhao, C. Li, R. Wang, D. Cao, G. Liu, Construction of Bi-assisted modified CdS/TiO_2 nanotube arrays with ternary S-scheme heterojunction for photocatalytic wastewater treatment and hydrogen production, Fuel 322 (2022) 124163, https://doi.org/10.1016/j.fuel.2022.124163.

[45] Y. Jia, P. Liu, Q. Wang, Y. Wu, D. Cao, Q.A. Qiao, Construction of Bi_2S_3-BiOBr nanosheets on TiO_2 NTA as the effective photocatalysts: pollutant removal, photoelectric conversion and hydrogen generation, J. Colloid Interface Sci. 585 (2021) 459–469, https://doi.org/10.1016/j.jcis.2020.10.027.

[46] Q. Wang, H. Li, X. Yu, Y. Jia, Y. Chang, S. Gao, Morphology regulated Bi_2WO_6 nanoparticles on TiO_2 nanotubes by solvothermal Sb^{3+} doping as effective photocatalysts for wastewater treatment, Electrochim. Acta 330 (2020) 135167, https://doi.org/10.1016/j.electacta.2019.135167.

[47] Z. Liu, Y. Song, Q. Wang, Y. Jia, X. Tan, X. Du, S. Gao, Solvothermal fabrication and construction of highly photoelectrocatalytic TiO_2 NTs/Bi_2MoO_6 heterojunction based on titanium mesh, J. Colloid Interface Sci. 556 (2019) 92–101, https://doi.org/10.1016/j.jcis.2019.08.038.

[48] J. Cao, B. Xu, B. Luo, H. Lin, S. Chen, Novel BiOI/BiOBr heterojunction photocatalysts with enhanced visible light photocatalytic properties, Catal. Commun. 13 (2011) 63–68, https://doi.org/10.1016/j.catcom.2011.06.019.

[49] C. Tian, H. Zhao, H. Sun, K. Xiao, P. Keung Wong, Enhanced adsorption and photocatalytic activities of ultrathin graphitic carbon nitride nanosheets: kinetics and mechanism, Chem. Eng. J. 381 (2020), https://doi.org/10.1016/j.cej.2019.122760.

[50] R. Hao, G. Wang, H. Tang, L. Sun, C. Xu, D. Han, Template-free preparation of macro/mesoporous g-C_3N_4/TiO_2 heterojunction photocatalysts with enhanced visible light photocatalytic activity, Appl. Catal. B Environ. 187 (2016) 47–58, https://doi.org/10.1016/j.apcatb.2016.01.026.

[51] D. Zhang, G. Tan, M. Wang, B. Li, A. Xia, The enhanced photocatalytic activity of Ag-OVs-(001) BiOCl by separating secondary excitons under double SPR effects, Appl. Surf. Sci. 526 (2020) 146689, https://doi.org/10.1016/j.apsusc.2020.146689.